Nanoscale

PAPER

View Article Online
View Journal | View Issue

Cite this: *Nanoscale*, 2025, **17**, 10269

Uncovering the electrocatalytic potential of two-dimensional Pt–Ni bimetallic aerogels†

Pavel Khavlyuk,[a] Fiona Tenhagen,[a] Yuanwu Liu,[a] René Hübner,[b] Volodymyr Shamraienko,[a] Johannes Kresse,[a] Angelika Wrzesińska-Lashkova,[c,d] Yana Vaynzof[c,d] and Alexander Eychmüller*[a]

Received 11th January 2025,
Accepted 26th March 2025

DOI: 10.1039/d5nr00133a

rsc.li/nanoscale

Metal aerogels have established themselves as promising materials for various applications across diverse fields, from sensing to soft neural implants. Since they emerged as a distinct class of materials in 2009, catalysis has been one of their most common application areas. However, even after a decade of research on metal aerogels for catalytic purposes, there remains room for improvement. The rising costs associated with production, driven by expensive drying techniques and costly metal precursors, have motivated the scientific community to explore alternative approaches and materials. This work investigates a film-like 2D Pt–Ni aerogel as a potential alternative for the methanol oxidation reaction (MOR). This aerogel was fabricated using a recently reported phase-boundary gelation, which requires a low quantity of metal precursors and avoids the need for special drying techniques. Comparative studies of the 2D and 3D aerogels confirm their structural integrity and the characteristic high porosity. The 2D Pt–Ni aerogel demonstrates a reproducibly high electrochemically active surface area of approximately 50.6 m^2 g^{-1} and an excellent mass activity for MOR of around 1.8 A mg^{-1}, surpassing the 3D Pt–Ni aerogel.

Introduction

Over the last decades, metal aerogels have become versatile materials with applications in various scientific and technological fields.[1,2] Their open pore network, the chemical nature of metals, as well as the ability to modify their surfaces and deposit them on substrates without binder or additives provide various opportunities in the field of catalysis, sensing, and energy storage.[3–5] More commonly, aerogels exhibit an irregular pore structure, containing both micropores and mesopores, as well as macropores larger than 50 nm in width.[6] This differentiates aerogels from other highly porous materials based on pore size, including microporous materials such as zeolites[7] and metal–organic frameworks,[8,9] and macroporous engineering materials,[10,11] with more or less fixed pore widths. The high surface area and open pore system of metal aerogels are directly related to their catalytic activity and electrochemical active surface area (ECSA), facilitating rapid diffusion of molecules within the structure, accelerating mass transport, and providing a large number of active surfaces and sites.

It was shown that the catalytic properties can be tailored by varying the morphological and structural form of the functional building blocks. In studies by Wang *et al.*, aerogels made of Pd metallene (perforated sheets) exhibit better catalytic performance than those made of Pd nanoparticles (NPs).[12] This enhancement in performance is assumed to be attributed to abundant active sites that are present in the film-like building blocks. In addition to this, different compositions with various element distributions can be tailored for specific reactions, where the incorporation of Pb in Pd metallene aerogels can lead to highly selective and stable electrochemical oxidation of polyalcohol.[13] Similarly to metal aerogels, adjusting the composition and elemental distribution allows tuning of the electronic structure, which alters adsorption energies and enhances electrocatalytic performance.[14,15] This approach was investigated for different aerogel compositions, such as Ag/Pt/Pd alloys,[16] Au–Pt alloys,[17] Pt–Ni alloys,[18] Pt–Bi core–shell,[19] Pd–Bi alloys,[20] and Ru–Au alloys.[21]

Significant progress has been made in improving the catalytic performance of Pt-based catalysts. Alloying Pt with another metal maximizes the intrinsic activity of each exposed

[a]*Physical Chemistry, Technische Universität Dresden, Dresden, 01069, Germany. E-mail: alexander.eychmueller@tu-dresden.de*
[b]*Institute of Ion Beam Physics and Materials Research, Helmholtz-Zentrum Dresden-Rossendorf e.V., Bautzner Landstrasse 400, 01328 Dresden, Germany*
[c]*Leibniz Institute for Solid State and Materials Research (IFW) Dresden, Helmholtzstraße 20, 01069 Dresden, Germany*
[d]*Chair for Emerging Electronic Technologies, Technische Universität Dresden, Nöthnitzer Str. 61, 01187 Dresden, Germany*

†Electronic supplementary information (ESI) available: SEM images of the 2D and 3D Pt–Ni aerogels, an XRD pattern of the 3D Pt–Ni aerogel, XPS survey and O 1s spectra of the 2D and 3D Pt–Ni aerogels, and top-down and cross-sectional SEM images of the 8-layered 2D Pt–Ni aerogel. See DOI: **https://doi.org/10.1039/d5nr00133a**

active site, significantly enhancing catalytic performance.[22] Moreover, some Pt alloys exhibit better selectivity toward desired products in alcohol oxidation and facilitate the removal of poisoning intermediates, such as CO, through a bifunctional mechanism.[23] However, while alloying Pt enhances the overall activity, it may reduce the ability of Pt to break C–C bonds in higher alcohols, such as ethanol.[24]

The application of alloyed Pt-based metal aerogels in catalysis was investigated thoroughly, since catalysis is essential in real life applications, making processes like fuel production and pollution control more efficient, cost-effective, and environmentally friendly.[25,26] However, despite this tremendous progress, several challenges still need to be addressed in the fabrication of metal aerogels.[18,19,27,28] Some of these challenges relate to the costs of Pt-based aerogels. One important aspect is the price of the main precursor, which is typically a noble metal salt, that incurs high production costs. Consequently, some research has focused on reducing the amounts of precursors needed during the synthesis or substituting them with less-expensive materials.[25] Another factor influencing production costs is the drying process, which often relies on using CO_2 gas or liquid nitrogen. However, these methods' environmental impact and energy consumption are major drawbacks, necessitating research into more cost-effective drying alternatives.[29] Overcoming these challenges is crucial for the industrial production of metal aerogels.

All these obstacles have led to the idea of finding new ways to prepare and apply metal aerogels. One approach is the preparation of two-dimensional (2D) metal aerogels *via* the recently reported phase-boundary gelation.[30,31] This approach holds potential for industrial applications, as it can be scaled to required sizes without the need for expensive equipment like supercritical or freeze dryers. Moreover, the 2D aerogels are electrically conductive to a certain degree and, due to their dimensionality, are expected to have a larger ECSA. A high surface area is crucial for aerogels in electrochemical applications, as it greatly influences their capacity to facilitate reactions, store energy, and transfer ions and electrons effectively.[25]

Herein, we report a reproducible methodology to synthesize 2D Pt–Ni aerogels *via* phase-boundary gelation, requiring less precursor and not needing expensive drying techniques than previously reported methods.[18,32] The properties of the 2D Pt–Ni aerogel were also compared to its three-dimensional (3D) counterpart in terms of structure and morphology. In addition, for the first time, electrochemical investigations of the 2D metal aerogel were performed toward the methanol oxidation reaction (MOR), showing enhanced mass activity compared to the 3D Pt–Ni aerogel.

Experimental

Materials

H_2PtCl_6 (8 wt% in H_2O, Sigma Aldrich), $NiCl_26{\cdot}H_2O$ (99%, Sigma Aldrich), $NaBH_4$ (purum p.a., ≥96% ((gas-volumetric), Sigma Aldrich), H_2SO_4 (95%, Alson Corp SE), *tert*-butanol (≥99.5%, Thermo Scientific), ethanol (≥99.8%, Fluka), and toluene (≥99.8%, Fluka) were used as received. MilliQ® water (0.056 μS cm^{-1}) was provided by a coupled system of RiOs™ 8 and Milli-Q Academic from Millipore.

Synthesis of aerogels

Pt–Ni NPs were prepared based on a modification of the previously established method by Henning *et al.*[32] Specifically, 74 μL of a 0.2 M H_2PtCl_6 solution and 510 μL of a 10 mM $NiCl_2$ solution were dissolved in 100 mL of water and stirred for 10 minutes. Next, 890 μL of freshly prepared cold 0.1 M $NaBH_4$ were added under vigorous stirring (450 rpm). After the solution changed to a dark brown color, it was stirred for an additional 30 minutes (450 rpm) and left to mature for 12 hours.

The 2D Pt–Ni aerogel was prepared using a stamping method, as described previously.[31] Briefly, 400 μL of the Pt–Ni NP solution were placed onto a cover glass with high surface tension. Then, 100 μL of an organic solvent mixture – toluene/ethanol (1 : 1) – were injected into the NP solution, creating two phases and initiating gelation at the phase boundary. After approximately 5 minutes, the organic phase evaporated at room temperature (around 20 °C), leaving a 2D network floating atop the water phase. This network was subsequently transferred to different substrates for further analysis; copper-coated grids for transmission electron microscopy (TEM), high-resolution TEM (HR-TEM) and scanning TEM (STEM) coupled with spectrum imaging analysis based on energy-dispersive X-ray spectroscopy (EDXS), indium tin oxide substrates for X-ray photoemission spectroscopy (XPS), silica wafers for scanning electron microscopy (SEM) and powder X-ray diffraction (XRD), and glass substrate for inductively coupled plasma optical emission spectroscopy (ICP-OES). The substrates were then dried overnight at room temperature under ambient conditions without further modification. The samples for XRD were prepared by stamping 30 layers (around 80 μg) of the 2D Pt–Ni aerogels. For the electrochemical investigations, all areas of the working electrode, except the surface to be loaded, were covered with Parafilm to prevent contamination during the modification process. After each layer addition, the electrode was rinsed with ethanol and dried with nitrogen gas for approximately 5 minutes. The procedure was repeated multiple times to achieve an optimized mass loading of 8 layers, at which a stable signal was observed.

For the preparation of 3D Pt–Ni aerogel, the same Pt–Ni NP solution used for the gelation of 2D Pt–Ni aerogels were left for 3 days at room temperature (20 °C) and a room humidity of 40%, during which a black hydrogel formed at the bottom of the beaker. The resulting 3D Pt–Ni hydrogel was carefully washed with water seven times, followed by a stepwise exchange of the water with *tert*-butanol, repeated five times. The solvogel was then freeze-dried to yield the 3D Pt–Ni aerogel. TEM, STEM-EDXS, XPS, and SEM samples of the 3D aerogel were prepared by dispersing the dried aerogel in water and drop-casting it onto the respective substrates.

Instruments and characterization

The nanostructure of the gels was investigated by TEM imaging using a JEOL/EO JEM1400plus with an LaB_6 cathode at an accelerating voltage of 120 kV. High-resolution TEM images were recorded using an image-Cs-corrected Titan 80–-300 microscope (FEI) operated at an accelerating voltage of 300 kV. Their homogeneity and porous structure were then checked by SEM imaging using a Hitachi FESEM SU8020 (3 kV, 7 mA). Cross-sectional SEM images were captured using the same operation parameters as for top-down SEM, but on specimen holders with a 90° profile. To characterize the chemical composition of the synthesized aerogels, high-angle annular dark-field STEM (HAADF-STEM) imaging and spectrum imaging analysis based on EDXS were performed on a Talos F200X microscope operated at 200 kV and equipped with an X-FEG electron source and a Super-X EDX detector system (FEI). Prior to the STEM analysis, the specimen mounted on a high-visibility, low-background holder was placed for 2 s into a model 1020 Plasma Cleaner (Fischione) to remove potential contaminations. The phase composition and crystallinity of the individual gels were investigated by powder XRD using a Bruker Phaser D2 (Cu-Kα = 1.5406 Å) diffractometer. XPS measurements were performed using an XR6 monochromatized Al-Kα source ($h\nu$ = 1486.6 eV) and a pass energy of 20 eV. Additionally, a flood gun was used in order to prevent charging. The binding energy scale was internally referenced to the C 1s peak at 285 eV. The samples for ICP-OES were prepared by dissolving the 2D Pt–Ni aerogel (8 layers on glass substrate) in 1.5 mL aqua regia, with subsequent removal of the glass substrate and dilution up to 15 mL with Milli-Q water. The analysis was done on a Thermo Fisher iCap7000 instrument to quantify the amount of Pt and Ni in the 2D aerogel. The weight per area of the deposited aerogel was then recalculated from the covered area, which was 0.1 cm^2 for Pt_3Ni.

ECSA and mass activity measurements were conducted in a three-electrode setup comprising a glassy carbon working electrode (diameter = 5 mm), an Ag/AgCl reference electrode (3.5 M KCl), and a Pt counter electrode, at room temperature. The system was controlled by a PGSTAT302 potentiostat/galvanostat from Autolab. The 2D Pt–Ni aerogel was layered onto the working electrode until a stable response was achieved, around 8 layers (approximately 2.7 μg). For preparing electrodes with the 3D Pt–Ni aerogel, 3.4 μl of a 0.642 mg mL^{-1} dispersion were drop-cast onto the glassy carbon surface and dried under nitrogen gas at room temperature. Cyclic voltammetry (CV) measurements were conducted over a potential range of −0.23 to 1.35 V with a scan rate of 50 mV s^{-1}, and each measurement was repeated at least three times to ensure reproducibility. The CV curves were mass-normalized based on the platinum loading to ensure an accurate comparison of the electrocatalytic activity. Electrochemical impedance spectroscopy (EIS) of catalysts was measured at 0.4 V (*vs.* RHE) in 0.5 M H_2SO_4 + 0.5 M methanol with frequency range from 0.1 to 105 Hz.

The ECSA (m^2 g^{-1}) of the aerogels was calculated by integrating the hydrogen adsorption/desorption region in the CV curves within the potential range of −0.217 to 0.105 V at a scan rate of 50 mV s^{-1}. The calculation assumed that the charge associated with a monolayer of hydrogen adsorbed on Pt is 210 μC cm^{-2}, following the established equation:[33]

$$\mathrm{ECSA} = \frac{q}{\Gamma L} = \frac{Q}{\Gamma L \nu}$$

q – area under the hydrogen adsorption/desorption region divided by the scan rate; Γ – specific capacitance (μC cm^{-2}); L – mass loading (μg cm^{-2}); ν – scan rate (mV s^{-1}); Q – charge from the hydrogen adsorption or desorption region.

Results and discussion

Structure characterization

The 2D bimetallic aerogel was synthesized by co-reducing the respective metal ions, followed by phase-boundary gelation, as described in the Experimental section. The morphology of this bimetallic aerogel was investigated by TEM. As shown in Fig. 1, both the 2D and 3D Pt–Ni aerogels consist of a mesh-like structure. The same characteristics can be seen in the SEM images in Fig. S1.† The Pt–Ni aerogel network consists of elongated particles, which form curvy shapes throughout the structure.

The average diameter of the wires is 4.6 nm for the 2D Pt–Ni aerogel, which is slightly smaller than the 5.6 nm of the 3D aerogel. The reduction in wire size for the 2D aerogel is connected to the fabrication method. Thoni *et al.* stated that during the freeze-drying process, the formation of small ice

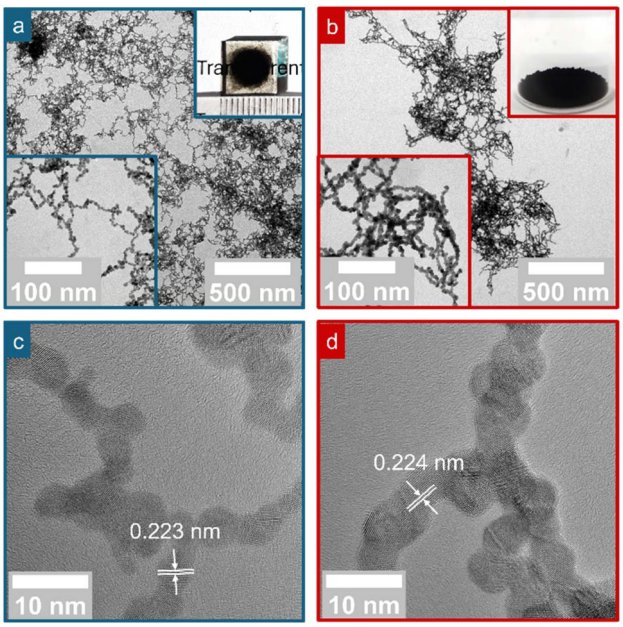

Fig. 1 TEM images of the (a) 2D and (b) 3D Pt–Ni aerogels at different magnifications, with the macroscopic appearance of the aerogels shown in the upper-right insets. HR-TEM images of the (c) 2D and (d) 3D Pt–Ni aerogels.

crystals within the gel network causes the unification of gel strands, resulting in a thicker web structure.[34] Another reason for the smaller wire size lies in the fabrication of the 2D aerogel, which occurs at the liquid–liquid interface and is governed by the Marangoni effect. The 2D Pt–Ni aerogels form through nanoparticle attachment, influenced by surface tension gradients at the water–oil interface and the addition of ethanol, which induces dipole–dipole interactions leading to wire-like structures.[35,36] Further growth occurs *via* surface atom diffusion and DLVO-driven aggregation, resulting in smooth, elongated networks rather than particle-to-particle assemblies.[37,38] This size-dependent phenomenon allows smaller particles with fewer charges to be trapped at the interface.[39] HR-TEM imaging in Fig. 1(c and d) reveals a lattice spacing of approximately 0.223 nm for both 2D and 3D Pt–Ni aerogels, corresponding to the (111) plane of Pt–Ni alloys.[40] Moreover, the network contains abundant grain boundaries, which are believed to enhance electrocatalytic performance.[41]

In bimetallic aerogels, the distribution of elements, specific composition, and morphology are of paramount importance, as they can significantly enhance the performance of the aerogels for targeted applications.[15] Tuning the composition is achievable by altering the mole ratios between the metal salts. The nominal composition of the 2D Pt–Ni aerogel was set to 75 : 25 (Table S1†). The atomic percentages obtained through ICP-OES analysis of the synthesized bimetallic aerogel closely matches this nominal composition, showing that the atomic ratio of Pt to Ni is 78 : 22. The STEM-EDX results are consistent with these findings, showing that the elemental quantification results for both 2D and 3D Pt–Ni aerogels are the same within the standard deviation.

Moreover, STEM-EDXS analysis (Fig. 2) showed the growth of the 2D bimetallic aerogel, revealing a concentration gradient in the element distribution, with Ni predominantly concentrated at the center of the wire and a minor presence on the surface. Both the 2D and 3D Pt–Ni aerogels exhibit a relatively homogeneous distribution of the elements within the network, with Ni enriched in the core and Pt enriched on the surface of the ligaments. This segregation behaviour has also been observed in other bimetallic aerogels prepared using a one-step approach, such as Au–Ir and Au–Rh.[42] It was attributed to a difference in the reaction kinetics of the salts, where faster formation of gold cores and slower nucleation of other metals on the surface were observed. Another potential factor influencing this behaviour is the difference in molar ratios. The element distribution in the aerogels presented in this work is comparable to previous studies on low Pt-containing Pt–Ni 2D aerogel.[22] In earlier work, the concentration gradient in the element distribution was attributed to an interdiffusion process governed primarily by the faster-diffusing species, with Ni dominating diffusion in the Pt–Ni aerogel.[43] Hence, Ni is predominantly concentrated in the center of the wires, with a minor presence on the surface, due to the slower diffusion of Pt compared with Ni. However, further investigations are needed to conclusively determine the underlying mechanisms. The diffraction pattern of the 3D and 2D aerogels, examined by XRD, confirms their *fcc* structure, with a small presence of NiO (Fig. S2†). The diffraction peaks are intermediate between the reference peaks of the parent metals and shifted in accordance with Vegard's law.[44]

Further physiochemical characterization

The chemical composition of both the 2D and 3D bimetallic aerogels was further investigated by XPS. The XPS survey scans of the 2D and 3D Pt–Ni aerogels, shown in Fig. S3a,† reveal the presence of Pt and Ni, along with impurities such as oxygen and carbon. The high-resolution Pt 4f XPS spectra depicted in Fig. 3a show two bands at 71.1 and 74.3 eV for both the 2D and 3D Pt–Ni aerogels; these are typically assigned to Pt $4f_{7/2}$ and Pt $4f_{5/2}$, respectively. The spectra were fitted with two doublets corresponding to Pt^0 and Pt^{2+}, assigned to PtO and $Pt(OH)_2$ species.[45]

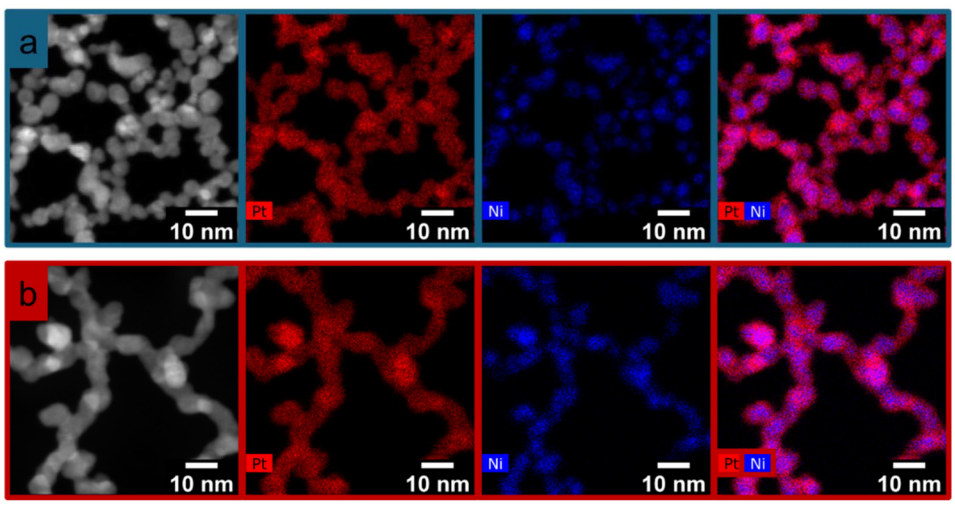

Fig. 2 HAADF-STEM images and corresponding EDXS-based element distribution maps of the (a) 2D and (b) 3D Pt–Ni aerogels.

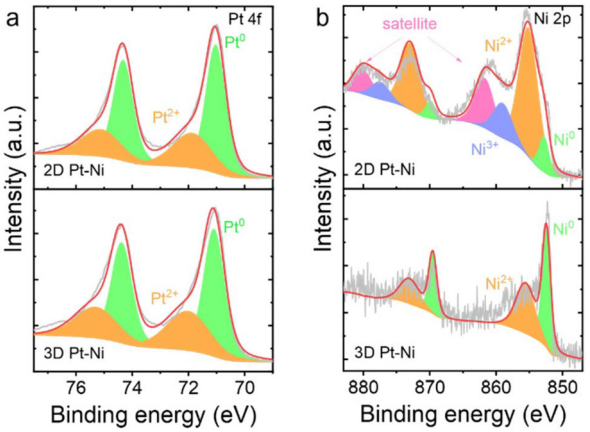

Fig. 3 XPS spectra of (a) Pt 4f and (b) Ni 2p core levels for the 2D and 3D Pt–Ni aerogels.

The XPS spectrum of Ni is shown in Fig. 3b. The Ni states of the 3D Pt–Ni aerogel consist of four bands at 852.5 and 869.4 eV and 869.4 eV for Ni^0 and 855.8 and 873.3 eV for Ni^{2+}.[46,47] In comparison, the Ni states in the 2D Pt–Ni aerogel exhibit additional bands at 861.9 and 880.3 eV, attributed to satellite signals, and two at 859.2 and 877.7 eV, which is attributed to Ni^{3+} (assigned to species in Ni_2O_3 and NiOOH).[48,49] The stronger signal of these satellite signals in 2D Pt–Ni aerogel indicates the higher amount of nickel ions in an oxidic environment.[50] The presence of Ni^0 and Ni^{2+} is observed at the same binding energies as in the 3D Pt–Ni aerogel. However, the amount of Ni^{2+}, which is generally associated with oxidation, is much higher in the 2D than in the 3D aerogel. The formation of oxidized Ni species in Pt–Ni aerogels, as observed in the Ni 2p XPS results, is common for aerogels and can be explained by the oxidation of Ni species under specific conditions, such as exposure to air.[40,51] A closer look at the O 1s spectrum (Fig. S3b†) reveals two distinct binding peaks at 531.2 and 530.2 eV for both aerogels. The first peak indicates chemisorbed hydroxyl species on the surface while the second peak is associated with oxygen atoms bonded to metals.[52,53]

Overall, the XPS analysis confirms the presence of hydroxides, oxides, and pure metals in all aerogels. Interestingly, the oxidation of the material depends on its structural characteristics. The increase in the Ni^{2+} band and the appearance of trivalent Ni in the 2D Pt–Ni aerogel spectrum, compared to the 3D aerogel, suggest that the 2D Pt–Ni aerogel is more susceptible to oxidation. This finding is consistent with studies showing that alloyed Ni films have a high affinity for oxygen.[54] Additionally, previous research established that the presence of oxidized Ni species on the surface of Pt catalysts is a key factor contributing to OH group adsorption, which is crucial in oxidation reactions such as MOR.[55] NiOOH is known to be highly active for alcohol oxidation reactions (*e.g.*, ethanol and methanol oxidation).[32] Based on these findings, the Pt–Ni aerogels were further investigated for their potential in electrocatalytic reactions.

Methanol oxidation reaction catalysis

Before the electrocatalytic studies, ICP-OES analysis was employed to calculate the 2D aerogel loading. To achieve a stable signal and optimal loading, the 2D aerogel was modified on the working electrode and glass substrate several times, referred to here as "layers". Specifically, a stable signal was obtained for 8 layers of the 2D Pt–Ni aerogels, resulting in a loading of 2.7 μg, which corresponds to 25 μg cm^{-2}, matching the minimal loading required for Pt–Ni catalysts in fuel cell investigations.[32] Although expecting the same porous structure in 2D Pt–Ni aerogels as in freeze-dried aerogels is ambitious, we assume that the adhesion of the 2D aerogels to the substrate helps to prevent collapse due to capillary stress. This assumption is supported by both top-down SEM and cross-sectional SEM images of the 8-layered 2D Pt–Ni aerogel (Fig. S4 and S5†), dried under ambient conditions, confirm that the porous gel structure was preserved, consistent with previously reported findings that aerogels sprayed on the substrate retain their typical porous, interconnected structure even when dried under ambient conditions, which should lead to a similarly high specific surface area.[56]

Electrochemical measurements were conducted to investigate the electrocatalytic activity of the Pt–Ni aerogels in a 0.5 M H_2SO_4 electrolyte, and the following results are presented at the 10th cycle. A detailed methodology is provided in the Experimental section. Pt mass-normalized CV curves, shown in Fig. 4a, were used to examine the adsorption and desorption properties of the aerogels. Hydrogen adsorption/desorption occurs at potentials below 0.1 V, with sharper peaks observed in the CV profiles of the 2D aerogels, suggesting enhanced transport efficiency for the reactants and products.

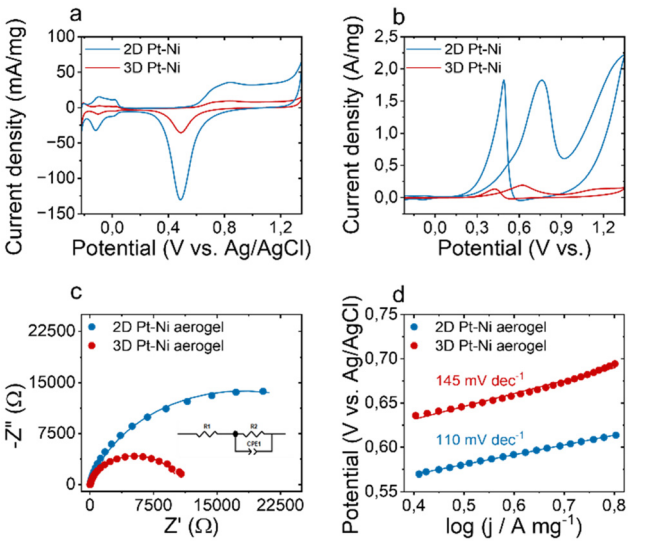

Fig. 4 Mass-normalized CV curves of the 2D and 3D Pt–Ni aerogels measured in (a) 0.5 M H_2SO_4 solution and (b) in a 0.5 M methanol + 0.5 M H_2SO_4 solution. (c) EIS Nyquist plots of 2D and 3D Pt–Ni aerogels measured in the frequency range of 0.1–10^5 Hz at a potential of 0.4 V (RHE). (d) Tafel plots derived from CV measurements.

The ECSAs were averaged from the hydrogen desorption charges.[18] The calculated ECSA values for the 3D and 2D Pt–Ni aerogels resulted in approximately 37.8, and 50.6 $m^2\ g^{-1}$, respectively. The ECSA value for the 3D Pt–Ni aerogel is consistent with previously reported values, while that for the 2D Pt–Ni aerogel is slightly higher than for 3D aerogels, indicating that more active sites are exposed in the 2D Pt–Ni aerogel.[18,57]

The MOR performance of the Pt–Ni aerogels was investigated by CV in a 0.5 M methanol + 0.5 M H_2SO_4 electrolyte. As shown in the noble metal mass-normalized CV curves in Fig. 4b, the currents display an anodic peak in the forward scan over the potential range from 0.3 to 0.9 V, corresponding to the oxidation of methanol.[55] Since the enhanced MOR activity is primarily attributed to the Ni, which alters the Pt d-band center and provides more oxygen-containing species at lower potentials facilitating the oxidation of adsorbed molecules. Additionally, the mass activity of the 2D Pt–Ni aerogel is higher than that of the 3D Pt–Ni aerogel, with 1.8 A mg^{-1} for the 2D aerogel and 0.2 A mg^{-1} for the 3D aerogel. As noted earlier, the 2D aerogel has more oxidized Ni species, which is crucial for MOR and contributes to its enhanced mass activity. As shown in Fig. 4d, the Tafel slope of the 2D Pt–Ni aerogel is only 110 mV dec^{-1}, which is lower than that of the 3D Pt–Ni aerogel 145 mV dec^{-1}, indicating that the 2D Pt–Ni has faster MOR kinetics.

Interestingly, the Nyquist plots of the catalysts measured at 0.4 V *versus* RHE are shown in the Fig. 4c show that both 2D and 3D Pt–Ni aerogels exhibit similar solution resistance, with R_1 values of 18.1 Ω and 18.9 Ω, respectively. However, the 3D Pt–Ni aerogel demonstrates a significantly lower charge-transfer resistance (R_2 = 10 644 Ω) compared to the 2D Pt–Ni aerogel (R_2 = 36 100 Ω), indicating enhanced electron transfer kinetics during the MOR. The increased charge transfer resistance may be attributed to the film-like appearance of the 2D aerogel likely affecting reaction kinetics. The high porosity of 3D aerogels facilitates better mass transport of reactants and products, reducing diffusion limitations and lowering charge transfer resistance.[25] Moreover, more oxidized Ni species can also decelerate the interfacial charge transfer process by forming insulating barriers between the catalyst surface and the electrolyte.[58,59]

A detailed investigation of the mechanism by which 2D aerogel facilitate electrochemical reactions, as well as a rigorous stability assessment involving comparisons of MOR activity before and after 5000 CV cycles, measurement of amperometric curves at a fixed overpotential, and analysis of the Pt–Ni structure *via* XRD or XPS to confirm the catalyst stability, is still needed but was beyond the scope of this study.

Summary and outlook

In summary, we successfully synthesized a 2D Pt–Ni aerogel, whereupon the synthetic methodology can be adapted for various metals and their combinations. XPS analysis revealed differences in surface composition between the 2D and 3D aerogels, with an increased oxide phase on the surface of the 2D aerogel compared to the 3D one, likely due to differences in surface structure exposure. This variation in surface oxide content contributes to differences in the catalytic properties of the aerogels. Electrochemical characterization demonstrated that the 2D aerogel could be a promising alternative to the 3D aerogel. The ECSA results of the 2D Pt–Ni aerogel (50.6 $m^2\ g^{-1}$) showed a significant increase compared to the 3D aerogel (37.8 $m^2\ g^{-1}$). A similar trend was observed for the MOR, with a mass activity of the 2D aerogel of 1.8 A mg^{-1}, compared to 0.2 A mg^{-1} for the 3D aerogel. This enhancement may be attributed to the higher content of oxidized Ni on the surface. Additional investigation of the kinetics showed that the 2D Pt–Ni aerogel exhibits a Tafel slope of just 110 mV dec^{-1}, lower than the 145 mV dec^{-1} of the 3D Pt–Ni aerogel, indicating enhanced MOR kinetics in the 2D structure. The higher charge transfer resistance of the 2D Pt–Ni aerogel suggests that its film-like structure impacts reaction kinetics, whereas the enhanced porosity of the 3D aerogel facilitates better mass transport and electron transfer. Additionally, the presence of oxidized Ni species may further hinder charge transfer by forming insulating barriers at the catalyst-electrolyte interface. This work shows that 2D Pt–Ni aerogels can be used as an alternative to 3D Pt–Ni aerogels in electrochemical reactions such as the MOR. The ability to produce 2D aerogels without expensive equipment, using fewer expensive precursors, and achieving increased performance makes them a highly promising material for future use in fuel cells and sensing. While the current investigation of structure parameters and electrochemical properties provides preliminary insight into the potential applications of the 2D aerogel in catalytic reactions, further studies, such as chronoamperometry, density functional theory calculations, and X-ray absorption spectroscopy, are needed to understand better the stability and reaction mechanisms of the 2D Pt–Ni aerogel.

Author contributions

P. K. and F. T. synthesized the Pt–Ni aerogels, prepared the samples, and conducted the XRD measurements. P. K. and V. S. conducted the TEM measurements and analysis. J. K. conducted the SEM measurements. R. H. conducted the STEM-based measurements and analyses. P. K., F. T., and Y. L. conducted the electrochemical measurements. A. W.-L. and Y. V. performed the XPS measurements and analyses. P. K., F. T., and A. E. wrote the paper. A. E. supervised the project. The authors have given approval to the final version of the manuscript.

Data availability

The data supporting this article have been included as part of the ESI.†

Conflicts of interest

There are no conflicts to declare.

Acknowledgements

We acknowledge the financial support from the German Research Foundation (DFG EY 16/30-1, RTG 2767 and CRC 1415, no. 417590517). We also thank Christine Steinbach for the ICP-OES measurements. Furthermore, the use of the HZDR Ion Beam Center TEM facilities and the funding of TEM Talos by the German Federal Ministry of Education and Research (BMBF; grant no. 03SF0451) in the framework of HEMCP are acknowledged.

References

1 A. Eychmüller, *J. Phys. Chem. C*, 2022, **126**, 19011–19023.
2 G. Li, C. Wang, Y. Chen, F. Liu, H. Fan, B. Yao, J. Hao, Y. Yu and D. Wen, *Small*, 2023, **19**, 2206868.
3 J. Yang, Y. Li, Y. Zheng, Y. Xu, Z. Zheng, X. Chen and W. Liu, *Small*, 2019, **15**, 1902826.
4 M. Fikry, J. Herranz, S. Leisibach, P. Khavlyuk, A. Eychmüller and T. J. Schmidt, *J. Electrochem. Soc.*, 2023, **170**, 114524.
5 W. Li, B. Weng, X. Sun, B. Cai, R. Hübner, Y. Luo and R. Du, *Catalysts*, 2023, **13**(1), 167.
6 M. A. Aegerter, N. Leventis, M. Koebel and S. A. Steiner III, *Springer Handbook of Aerogels*, Springer Nature, 2023.
7 M. Dusselier and M. E. Davis, *Chem. Rev.*, 2018, **118**, 5265–5329.
8 A. A. Moghadam, A. Rezvani, H. Saravani, M. Shahbakhsh and G. Sargazi, *Catal. Lett.*, 2024, **154**, 1828–1838.
9 N. Arab, L. Fotouhi, P. S. Dorraji and G. Sargazi, *J. Electroanal. Chem.*, 2020, **860**, 113923.
10 F. Zhang, Z. Li, M. Xu, S. Wang, N. Li and J. Yang, *J. Eur. Ceram. Soc.*, 2022, **42**, 3351–3373.
11 E. Babaie and S. B. Bhaduri, *ACS Biomater. Sci. Eng.*, 2018, **4**, 1–39.
12 C. Wang, W. Wei, M. Georgi, R. Hübner, C. Steinbach, Y. Bräuniger, S. Schwarz, S. Kaskel and A. Eychmüller, *ChemElectroChem*, 2024, **11**, e202400060.
13 H. Fu, Z. Huang, T. Zhu, L. Guan, C.-W. Pao, W.-H. Huang, N. Zhang and T. Liu, *ACS Mater. Lett.*, 2024, **6**, 4801–4809.
14 J. Kresse, M. Georgi, R. Hübner and A. Eychmüller, *Nanoscale Adv.*, 2023, **5**, 5487–5498.
15 C. Wang, J. Herranz, R. Hübner, T. J. Schmidt and A. Eychmüller, *Acc. Chem. Res.*, 2023, **56**, 237–247.
16 R. Sarkar, L. S. Graves, J. R. Taylor and I. U. Arachchige, *ACS Appl. Mater. Interfaces*, 2023, **15**, 50981–50993.
17 C. Wang, L. Wang, V. Nallathambi, Y. Liu, J. Kresse, R. Hübner, S. Reichenberger, B. Gault, J. Zhan, A. Eychmüller and B. Cai, *Adv. Mater.*, 2024, **36**, 2405200.
18 M. Fikry, N. Weiß, M. Bozzetti, S. Ünsal, M. Georgi, P. Khavlyuk, J. Herranz, V. Tileli, A. Eychmüller and T. J. Schmidt, *ACS Appl. Energy Mater.*, 2024, **7**, 896–905.
19 G. Xue, Y. Li, R. Du, J. Wang, R. Hübner, M. Gao and Y. Hu, *Small*, 2023, **19**, 2301288.
20 H. Wang, L. Jiao, L. Zheng, Q. Fang, Y. Qin, X. Luo, X. Wei, L. Hu, W. Gu, J. Wen and C. Zhu, *Adv. Funct. Mater.*, 2021, **31**, 2103465.
21 W. Wei, F. Guo, C. Wang, L. Wang, Z. Sheng, X. Wu, B. Cai and A. Eychmüller, *Small*, 2024, 2310603.
22 T. T. Huynh, Q. Huynh, Q. V. Nguyen and H. Q. Pham, *Inorg. Chem.*, 2023, **62**, 20477–20487.
23 H. Q. Pham and T. T. Huynh, *J. Phys. Chem. Lett.*, 2023, **14**, 4631–4637.
24 T. T. Huynh, Q. Huynh, A. Q. K. Nguyen and H. Q. Pham, *Adv. Sustainable Syst.*, 2025, 2400995.
25 B. Cai and A. Eychmüller, *Adv. Mater.*, 2019, **31**, 1804881.
26 H. Maleki and N. Hüsing, *Appl. Catal., B*, 2018, **221**, 530–555.
27 H. Wang, Q. Fang, W. Gu, D. Du, Y. Lin and C. Zhu, *ACS Appl. Mater. Interfaces*, 2020, **12**, 52234–52250.
28 R. Du, J. Joswig, R. Hübner, L. Zhou, W. Wei, Y. Hu and A. Eychmüller, *Angew. Chem.*, 2020, **132**, 8370–8377.
29 R. Garrido, J. D. Silvestre, I. Flores-Colen, M. de F. Júlio and M. Pedroso, *J. Non-Cryst. Solids*, 2019, **516**, 26–34.
30 K. Hiekel, S. Jungblut, M. Georgi and A. Eychmüller, *Angew. Chem., Int. Ed.*, 2020, **59**, 12048–12054.
31 P. Khavlyuk, A. Mitrofanov, V. Shamraienko, R. Hübner, J. Kresse, K. B. L. Borchert and A. Eychmüller, *Chem. Mater.*, 2023, **35**, 2864–2872.
32 S. Henning, L. Kühn, J. Herranz, J. Durst, T. Binninger, M. Nachtegaal, M. Werheid, W. Liu, M. Adam, S. Kaskel, A. Eychmüller and T. J. Schmidt, *J. Electrochem. Soc.*, 2016, **163**, F998.
33 V. K. Ramani, K. Cooper, J. M. Fenton and H. R. Kunz, in *Springer Handbook of Electrochemical Energy*, ed. C. Breitkopf and K. Swider-Lyons, Springer Berlin Heidelberg, Berlin, Heidelberg, 2017, pp. 649–711.
34 L. Thoni, N. Metzkow and A. Eychmüller, *J. Sol-Gel Sci. Technol.*, 2023, **107**, 218–226.
35 D. E. Sanders and A. E. DePristo, *Surf. Sci.*, 1992, **260**, 116–128.
36 J. Liao, Y. Zhang, W. Yu, L. Xu, C. Ge, J. Liu and N. Gu, *Colloids Surf., A*, 2003, **223**, 177–183.
37 S. Lazzari, L. Nicoud, B. Jaquet, M. Lattuada and M. Morbidelli, *Adv. Colloid Interface Sci.*, 2016, **235**, 1–13.
38 S. Jungblut, J.-O. Joswig and A. Eychmüller, *Phys. Chem. Chem. Phys.*, 2019, **21**, 5723–5729.
39 M. Oettel, *Phys. Rev. E: Stat., Nonlinear, Soft Matter Phys.*, 2007, **76**, 041403.
40 X.-D. Tang, M. Zeng, D.-P. Chen, L. Yua, C.-Y. Wang, W. Li and Y. Yi, *ChemistrySelect*, 2021, **6**, 12696–12701.
41 Z. Zhang, Z. Luo, B. Chen, C. Wei, J. Zhao, J. Chen, X. Zhang, Z. Lai, Z. Fan, C. Tan, M. Zhao, Q. Lu, B. Li, Y. Zong, C. Yan, G. Wang, Z. J. Xu and H. Zhang, *Adv. Mater.*, 2016, **28**, 8712–8717.
42 R. Du, J. Wang, Y. Wang, R. Hübner, X. Fan, I. Senkovska, Y. Hu, S. Kaskel and A. Eychmüller, *Nat. Commun.*, 2020, **11**, 1590.
43 V. D. Divya, U. Ramamurty and A. Paul, *J. Mater. Res.*, 2011, **26**, 2384–2393.

44 T.-W. Chen, J.-X. Kang, D.-F. Zhang and L. Guo, *RSC Adv.*, 2016, **6**, 71501–71506.
45 X.-W. Zhou, R.-H. Zhang, Z.-Y. Zhou and S.-G. Sun, *J. Power Sources*, 2011, **196**, 5844–5848.
46 W. Xu, J. Chang, Y. Cheng, H. Liu, J. Li, Y. Ai, Z. Hu, X. Zhang, Y. Wang, Q. Liang, Y. Yang and H. Sun, *Nano Res.*, 2022, **15**, 965–971.
47 T. Cheng, Z. Wang, S. Fang, H. Jin, C. Zhu, S. Zhao, G. Zhuang, Q. Chen and Y. Zhu, *Nano Res.*, 2024, **17**, 9822–9829.
48 A. A. Dubale, Y. Zheng, H. Wang, R. Hübner, Y. Li, J. Yang, J. Zhang, N. K. Sethi, L. He, Z. Zheng and W. Liu, *Angew. Chem., Int. Ed.*, 2020, **59**, 13891–13899.
49 S. Y. Shen, T. S. Zhao, J. B. Xu and Y. S. Li, *J. Power Sources*, 2010, **195**, 1001–1006.
50 B. Pawelec, S. Damyanova, K. Arishtirova, J. L. G. Fierro and L. Petrov, *Appl. Catal., A*, 2007, **323**, 188–201.
51 Y. Zheng, A. S. Petersen, H. Wan, R. Hübner, J. Zhang, J. Wang, H. Qi, Y. Ye, C. Liang, J. Yang, Z. Cui, Y. Meng, Z. Zheng, J. Rossmeisl and W. Liu, *Adv. Energy Mater.*, 2023, **13**, 2204257.
52 Y. Wang, X. Di, J. Chen, L. She, H. Pan, B. Zhao and R. Che, *Carbon*, 2022, **191**, 625–635.
53 T. Li, T. Zheng, T. Hui, J. Pan, R. Zhang, H. Liu, Z. Liu, C. Xu and X. Meng, *Appl. Surf. Sci.*, 2024, **668**, 160397.
54 J. Eidhagen, A. Larsson, A. Preobrajenski, A. Delblanc, E. Lundgren and J. Pan, *J. Electrochem. Soc.*, 2023, **170**, 021506.
55 S. Lu, H. Li, J. Sun and Z. Zhuang, *Nano Res.*, 2018, **11**, 2058–2068.
56 P. Khavlyuk, V. Shamraienko, F. Tenhagen, J. Kresse, N. Weiß, N. Gaponik and A. Eychmüller, *J. Phys. Chem. C*, 2023, **127**, 12708–12716.
57 M. Fikry, Á. García-Padilla, J. Herranz, P. Khavlyuk, A. Eychmüller and T. J. Schmidt, *ACS Catal.*, 2024, **14**, 1903–1913.
58 D. Majumdar and S. K. Bhattacharya, *ChemistrySelect*, 2022, **7**, e202201807.
59 D. Yu, X. Zhang, K. Wang, L. He, J. Yao, Y. Feng and H. Wang, *Int. J. Hydrogen Energy*, 2013, **38**, 11863–11869.